ADVANCED MATERIALS INTERFACES
www.advmatinterfaces.de

Combinatorial Investigation and Modelling of MoO_3 Hole-Selective Contact in $TiO_2|Co_3O_4|MoO_3$ All-Oxide Solar Cells

*Koushik Majhi, Luca Bertoluzzi, Kevin James Rietwyk, Adam Ginsburg, David A. Keller, Pilar Lopez-Varo, Assaf Y. Anderson, Juan Bisquert, and Arie Zaban**

A $TiO_2|Co_3O_4|MoO_3$ all-oxide solar cell produced by spray pyrolysis and pulsed laser deposition (PLD) onto a fluorine-doped tin-oxide (FTO) glass substrate with gold (Au) back contacts is demonstrated for the first time. A combinatorial approach is implemented to study the effect of molybdenum oxide (MoO_3) as a recombination contact and the influence of the cobalt oxide (Co_3O_4) light-absorber thickness on the performance of the solar cells. An increase of more than 200 mV in the open circuit voltage (V_{oc}) is observed with a concurrent enhancement in terms of short-circuit current (J_{sc}) and maximum power in comparison with $TiO_2|Co_3O_4$ devices without the MoO_3 layer. To understand the mechanism, full drift diffusion simulations are performed. The higher performance is attributed to elimination of a recombination process at the absorber/metal back-contact interface and surface passivation by the MoO_3 layer.

1. Introduction

Metal–oxide (MO) semiconductors are regarded as an emerging class of materials to address the growing demand of low-cost solar cells.[1] Co_3O_4 is a very stable and earth-abundant metal oxide with intrinsic p-type conductivity and two optical band-gaps (≈1.5 eV and ≈2 eV) in the visible region.[2] The p-type nature of Co_3O_4 thin films has been successfully exploited to form efficient heterojunctions in many applications, including solar photocatalysis,[3] solar cells,[4] supercapacitors,[5] high-performance sensing devices,[6] and cathode materials for rechargeable lithium batteries.[7]

K. Majhi, K. J. Rietwyk, A. Ginsburg,
D. A. Keller, A. Y. Anderson, Prof. A. Zaban
Department of Chemistry
Center for Nanotechnology & Advanced Materials
Bar Ilan University
Ramat Gan 52900, Israel
E-mail: arie.zaban@biu.ac.i
L. Bertoluzzi, J. Bisquert
Institute of Advanced Materials (INAM)
Universitat Jaume I
12071 Castelló, Spain
Dr. P. Lopez-Varo
Departamento de Electrónica y Tecnología de Computadores
CITIC-UGR
Universidad de Granada
18071 Granada, Spain

DOI: 10.1002/admi.201500405

Co_3O_4 has a high work function (6.3 eV) and ionization potential (6.6 eV), which greatly limits the number of metals with appropriate energetic characteristics to act as effective contacts for hole extraction in devices.[8] The addition of hole-selective contacts (HSC) and hole-selective materials allows for better extraction of holes. A potential hole-selective material is MoO_3 – an n-type semiconductor with a large electron affinity (≈6.7 eV) and work function (≈6.9 eV), which rules out any electron transport via the conduction band[9] across the $Co_3O_4|MoO_3$ interface. However, the energy alignment between the conduction band minimum of MoO_3 and the valence band maximum of Co_3O_4 might be favorable for hole transfer from the Co_3O_4 valence band to the MoO_3 conduction band. Furthermore, little to no band bending is likely to occur at the interface due to the close proximity in work functions between these two materials.[8] We predict that a similar mechanism will occur as reported by Schulz et al. for the case of NiO_x/MoO_3 bilayers.[9] According to this mechanism, MoO_3 can form the basis of a "charge recombination" layer. Thus, holes can be extracted very effectively via recombination at the $Co_3O_4|MoO_3$ interface and collected at the metal back contacts. Clearly, this makes MoO_3 a suitable choice for serving as a hole-selective contact (HSC).[9,10]

Molybdenum oxide is widely used as a hole-selective contact (HSC) and has received significant attention for improving the performance and stability in organic and c-Si solar cells.[11–17] MoO_3 as a HSC reduces charge recombination by suppressing exciton quenching as well as the resistance at the photoactive layer|anode interface in organic solar cells.[18] The MoO_3 HSC also serves as an optical spacer for improving the light absorption, thereby enhancing the photocurrent.[15,19]

Molybdenum oxide was considered a p-type semiconductor[20] but recently ultraviolet photoemission spectroscopy studies have shown that it is a n-type semiconductor.[21,22] With a high work function exceeding those of elemental metals, MoO_3 offers opportunities for hole contact in inorganic semiconductor materials with layered transition metal dichalcogenide semiconductors as well as carbon-based nanomaterials.[23–25]

In this report we introduce molybdenum oxide, deposited by pulsed laser deposition, as a recombination contact in Co_3O_4-based all-oxide photovoltaic cells. The research methodology involves combinatorial device libraries that are characterized for

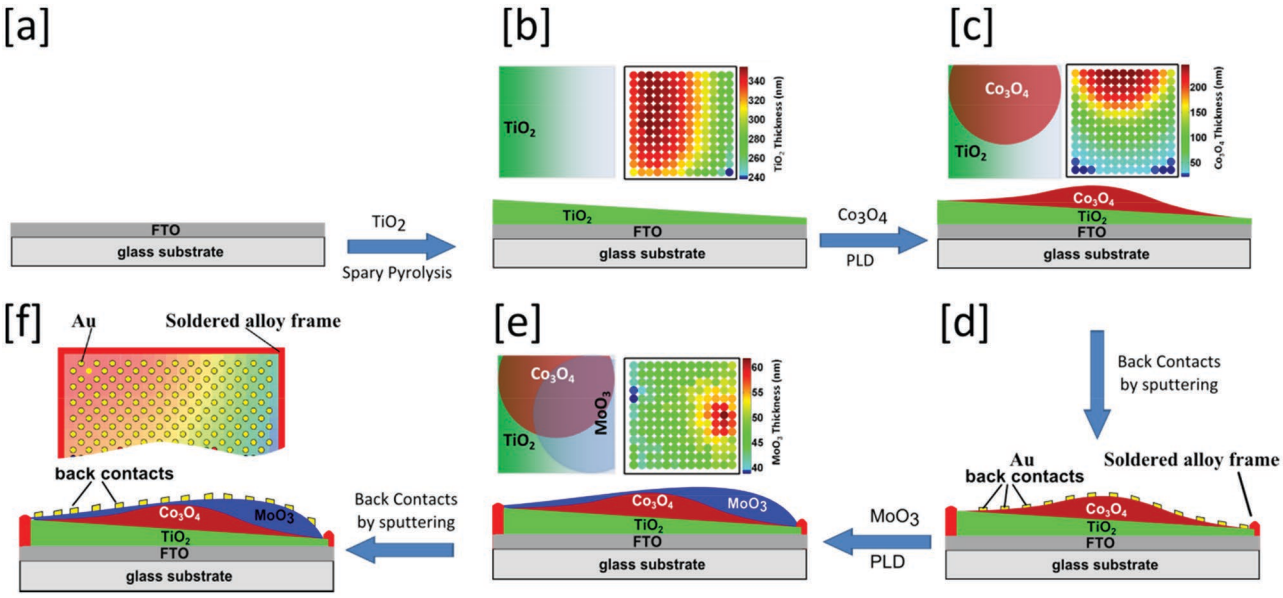

Figure 1. Schematic representation of the preparation of combinatorial $TiO_2|Co_3O_4|Au$ and $TiO_2|Co_3O_4|MoO_3|Au$ libraries. FTO-covered glass (Figure 1a) onto which a TiO_2 layer was deposited with a linear thickness gradient indicated in blue with the thickness profile of the corresponding layers displayed on the top (Figure 1b). The Co_3O_4 absorber layer was deposited by pulsed laser deposition (PLD) perpendicular to the TiO_2 thickness gradient with the thickness profile of the corresponding layers displayed on the top (Figure 1c). A grid of 13×13 100-nm thick metal circles with diameters of 1.8 mm were deposited by sputtering onto the Co_3O_4 layer using a shadow mask which served as back contacts and cross-section of combinatorial PV device library (Figure 1d). A MoO_3 thin film was deposited onto the same Co_3O_4 layer with an additional grid of Au back contacts (offset to the original grid). It was deposited in a continuous thickness gradient perpendicular to the Co_3O_4 deposition profile using PLD with the thickness profile of the corresponding layers. The layers are displayed on the top and cross-section of combinatorial PV device library shown on top (Figure 1e). Back contact arrangement on the top and cross-section of combinatorial PV device library (Figure 1d and f).

their chemical, structural, optical, and electrical properties.[26–28] We show that a thin layer of MoO_3 inserted between the Co_3O_4 absorber and the metal back contact improves the photovoltaic performance. With the help of advanced modeling and calculations, we have demonstrated improvements in the performance by removing the surface recombination center and passivation on the oxide–metal back contact interface.

2. Results

Figure 1 shows schematic diagrams of the combinatorial $TiO_2|Co_3O_4|Au$ and $TiO_2|Co_3O_4|MoO_3|Au$ device libraries. FTO-covered glass substrates serve as a joint front electrode onto which the TiO_2 layer was deposited with a linear thickness gradient indicated by the green color (Figure 1b) that varied

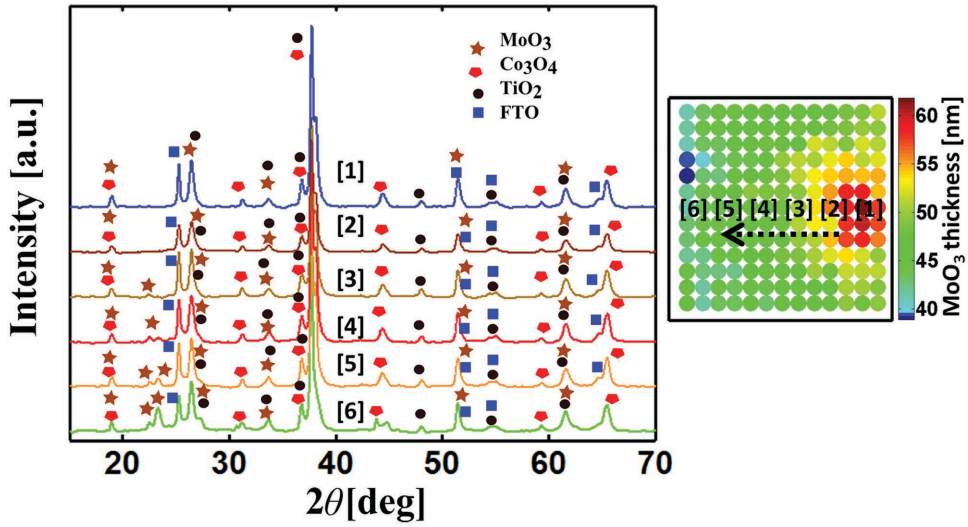

Figure 2. X-ray diffraction patterns for the $Co_3O_4|MoO_3$ device film deposited onto compact TiO_2 on FTO-coated glass. The labelling of the XRD spectra correlates to the spatial position on the PV library, as shown in the image on the right. The main diffraction peaks marked by a pentagon are assigned to the Co_3O_4 polycrystalline phase with a cubic structure (Fm3m).

from 240 to 340 nm. This was followed by the Co_3O_4 absorber layer indicated in red (Figure 1c). A MoO_3 thin film was deposited onto the same Co_3O_4 layer with an additional grid of Au back contacts (offset to the original grid). It was deposited in a continuous thickness gradient perpendicular to the Co_3O_4 deposition profile using PLD and MoO_3 layer indicated in blue (Figure 1e) recombination contact layers, both with bell-shaped gradients perpendicular to each other. The thickness of the Co_3O_4 and MoO_3 layers changed from 40 to 250 nm (Figure 1c) and 35 to 65 nm (Figure 1e), respectively. Figure 1d and 1f show the back contact arrangement and the cross-section of the combinatorial PV device library.

Figure 2 depicts the X-ray diffraction patterns (XRD) for the $TiO_2|Co_3O_4|MoO_3|Au$ device libraries along the MoO_3 thickness gradient as shown in the right hand image, where the numbers show the position in the PV library where the XRD pattern was recorded (right to left in the direction of decreasing MoO_3 thickness indicated by the arrow). The XRD measurements show pronounced peaks of MoO_3, Co_3O_4, and TiO_2 as indicated in the plots. The relative intensities of the Co_3O_4, and SnO_2 peak remain constant from right to left across the library, because the thickness of these layers remains constant in this direction.

Figure 3 depicts *I–V* characteristics of the $TiO_2|Co_3O_4|Au$ and $TiO_2|Co_3O_4|MoO_3|Au$ device libraries in order to enable a comparison of the performance of the cells with and without the MoO_3 layer. The first noticeable difference between the two libraries is the number of active photovoltaic cells. A higher number of active PV cells are present in the $TiO_2|Co_3O_4|MoO_3$ library than in the $TiO_2|Co_3O_4$ library. Secondly, the open circuit voltage (V_{oc}) is significantly enhanced upon addition of the MoO_3 layer, from 450 to 660 mV (note the change of the voltage color scale). Thirdly, the region with the maximum short-circuit current, (J_{sc}) which is confined to the thick absorber region of the $TiO_2|Co_3O_4$ device library (Figure 3c), moved to the thinner part of the absorber layer for cells that contain the MoO_3 layer (Figure 3d).

The maximum power point (P_{max}) and internal quantum efficiency (IQE) follow a similar trend to the one for J_{sc}. The fill factor (FF) values for the library with MoO_3 are higher than that without MoO_3.

3. Discussion

Figure 4 displays the various PV parameters (V_{oc}, J_{sc}, FF, IQE and P_{max}) as a function of the absorber (Co_3O_4) thickness for $TiO_2|Co_3O_4|Au$ (blue dots) and $TiO_2|Co_3O_4|MoO_3|Au$ (green dots) to emphasize correlations between these parameters and the absorber layer thickness. For the $TiO_2|Co_3O_4|Au$ device library there is clear trend where each parameter improves with increasing absorber thickness. Both the J_{sc} and V_{oc} of this library show no maximum point over the thickness range shown here, suggesting that thicker absorbers could provide higher performance. However, another library with a Co_3O_4 absorber layer thicker than 250 nm (not shown here) revealed a decrease in performance, mainly with respect to J_{sc}.

The photovoltaic behavior of the $TiO_2|Co_3O_4|MoO_3|Au$ device library as a function of absorber thickness shows different trends to the library without the MoO_3 layer. In Figure 4a, V_{oc} increases from 200 mV and reaches a peak value of 660 mV at an absorber thickness of 50–60 nm . At an absorber thickness of >60 nm, V_{oc} starts decreasing with increasing absorber thickness and approaches a similar value to that observed in the $TiO_2|Co_3O_4|Au$ device library. We also note a decrease in the V_{oc} below 50 nm (Figure 4a), at the lowest absorber thickness. This may be associated with the pin holes that can correlate with the very low values of FF (Figure 4c). The FF increases with the increasing absorber thickness until reaching a maximum of 42% at an absorber thickness of 150 nm and then starts decreasing when the absorber thickness is further increased. The highest J_{sc} value can be observed for the absorber with a thickness range of 50–60 nm (Figure 4c). The maximum power

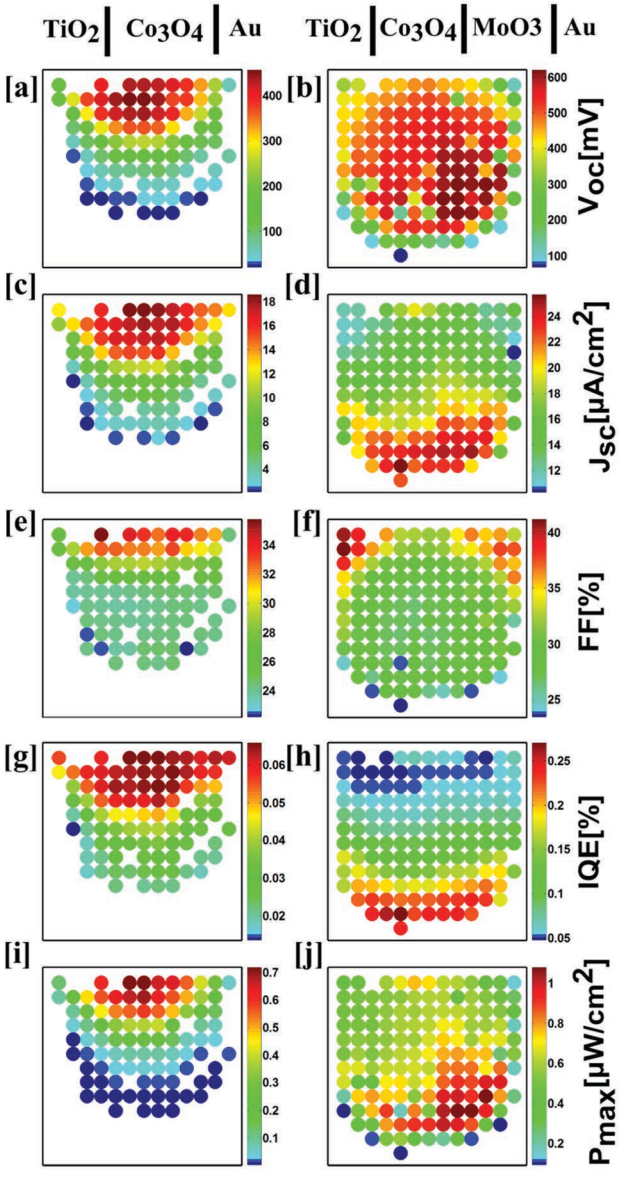

Figure 3. Maps of the open circuit voltage (V_{oc}), short circuit current (J_{sc}) and fill factor (FF), internal quantum efficiency (IQE [%]), and maximum power point (P_{max}) as a function of cell position in the library, for devices with (right rows) and without (left rows) a MoO_3 recombination contact layer. Each map represents cells with an Au back-contact material.

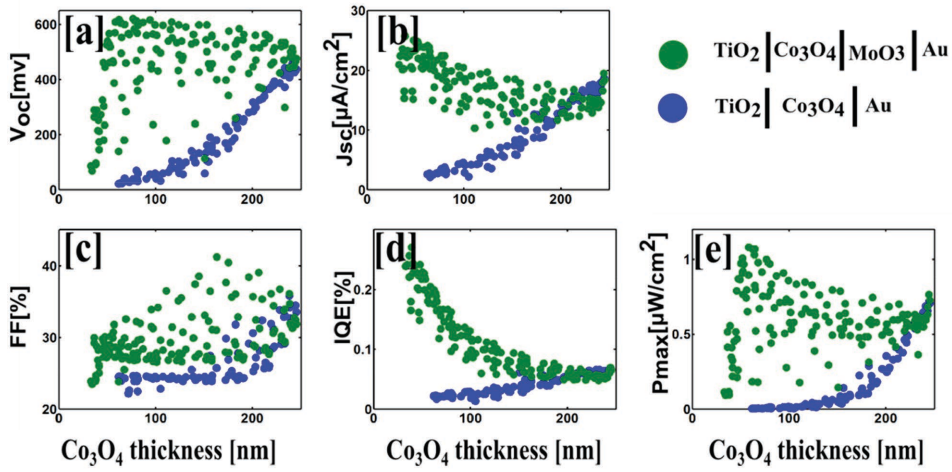

Figure 4. Plots of the V_{oc}, J_{sc}, FF, IQE, and P_{max} as a function of absorber layer thickness for libraries with (green solid dots) and without (blue solid dots) the MoO_3 hole-selective contact.

point, (P_{max}) (Figure 4e), which is the product of the maximum voltage and current, follows the same trend as V_{oc} and J_{sc}.

The IQE is an important parameter for this study and is defined as the ratio of the number of charge carriers that are photogenerated and collected in the solar cell to the number of photons that are observed by the cell. It provides a measure of the efficiency with which photons that are absorbed in the device can generate useful carriers that are collected at the contacts. The IQE is essentially normalized to the absorber thickness, enabling comparison between cells with different absorber thickness. The improvement of the IQE with increasing thickness for the absorber layer in the $TiO_2|Co_3O_4|Au$ device library suggests that the performance is limited by absorber surface/interface effects. In contrast to this, the $TiO_2|Co_3O_4|MoO_3|Au$ devices show a reduction in similar parameters with increasing absorber thickness, indicating the limitation is bulk-like in nature. In particular we attribute this limitation to the known poor transport characteristic ability through diffusion associated with the cobalt oxide (Co_3O_4) absorber.

The combinatorial study of the libraries with and without MoO_3 layer point towards poor absorber transport properties. During the fabrication of metal oxides, the abrupt termination of the crystal at surfaces and interfaces leads to an array of atoms with dangling bonds that are highly reactive. Since these materials are grown in poor vacuum conditions, these atoms readily bond to contaminations in the ambient environment resulting in a highly disordered surface with a high density of recombination centers. The presence of these recombination centers at surfaces/interfaces is detrimental to absorber transport properties. Deposition of MoO_3 on the absorber layer could eradicate these traps and work as a passivation layer.

In light of the previous analysis, we can make the four following assumptions with regard to the main processes that affect the photovoltaic performance of the devices studied in this work. i) The decay of V_{oc} and J_{sc} observed at larger thickesses for the $TiO_2|Co_3O_4|MoO_3|Au$ devices suggests a sluggish extraction of the minority carriers (i.e., electrons) at the electron-selective contact ($TiO_2|Co_3O_4$). ii) Due to the band alignment properties of the $Co_3O_4|Au$ and $Co_3O_4|MoO_3$ interfaces, we assume that surface recombination occurs at both interfaces. iii) A large density of surface states induces high recombination at the $Co_3O_4|Au$ interface. iv) These inner bandgap states can be removed by using an interlayer of MoO_3, which enhances the photovoltaic performance. To corroborate these assumptions, we have elaborated two models, presented in **Figure 5**, one for the $TiO_2|Co_3O_4|Au$ devices (Figure 5a) and the other one for the $TiO_2|Co_3O_4|$ $MoO_3|Au$ ones (Figure 5b).

According to hypothesis (i), we can assume that surface recombination occurs at the $TiO_2|Co_3O_4$ interface for both devices, which is modeled by the recombination velocity S_n. Similarly, according to assumption (ii), we have modeled surface recombination at the Co_3O_4 $|MoO_3$ (HSC) interface with the parameter S_p. In agreement with assumption (iii), we have considered a density of surface states, N_t, at the interface $Co_3O_4|Au$, where trap-assisted recombination can take place and induce current losses.[31] Finally, hypothesis (iv) states that there is no such density of surface states at the $Co_3O_4|MoO_3$ interface and we assume that $N_t = 0$. The other processes that we consider are common factors in both models: light-induced generation of free carriers and bulk recombination at rates G and U_r, respectively. The established modeling framework (Figure 5) allowed us to calculate the theoretical trends of J_{sc} and V_{oc} with the absorber thicknesses for both device configurations. Our calculations were performed using the full numerical drift-diffusion approach. The details of our equations are given in the Appendix (in the Supporting Information) and the results of our simulations are given in **Figure 6**.

Our simulations reproduce very well several of the features observed experimentally. Firstly, we can reproduce the current losses observed for the $TiO_2|Co_3O_4|MoO_3|Au$ devices, which validates assumption (i). We therefore infer that these devices undergo slow extraction of the minorities (electrons) at the TiO_2/semiconductor contact. Since electrons cannot be extracted efficiently, a concentration gradient builds up between the interface and the bulk of the semiconductor where electrons diffuse and recombine. This effect becomes more important as the thickness of the semiconductor increases, because the probability

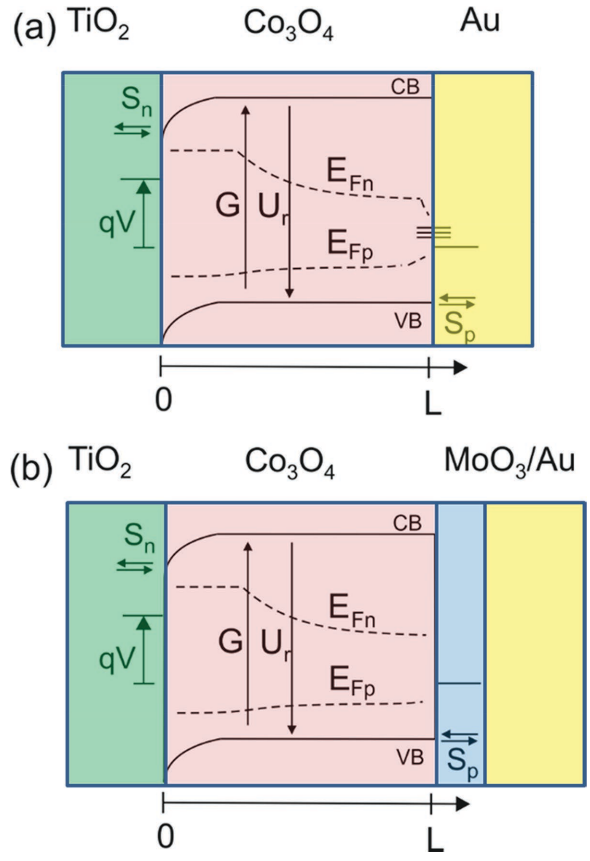

Figure 5. Schematic of the model used for our full drift diffusion simulations. Upon illumination from the TiO_2, free carriers are generated at a rate G and recombine at a rate U_r. At the electron-selective contact (ESC), for $x = 0$, surface recombination affects electron extraction at a rate S_n. Similarly, at the hole-selective contact (HSC), for $x = L$, holes are extracted at a rate S_p. The applied voltage is defined as the potential difference between the ESC ($x = 0$) and the HSC ($x = 0$). At the semiconductor/HSC interface we consider a) Shockley Read Hall recombination (the surface states are presented by horizontal lines at Co_3O_4/Au interface) in the case of the Co_3O_4|Au interface and b) simple hole transfer at the Co_3O_4|MoO_3 interface.

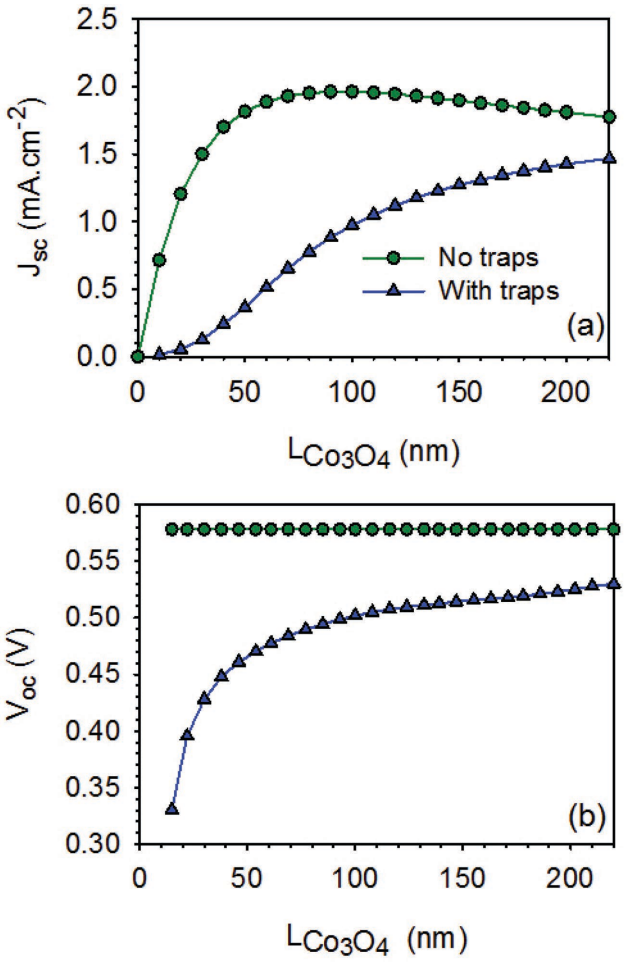

Figure 6. Simulation of a) the short circuit current (J_{sc}) and b) open circuit voltage (V_{oc}) for model (b) of Figure 5 (green plots) and for model (a) of Figure 5 (blue plots). The values of the parameters used for our simulations are given in the Table 1 of the Appendix.

of recombination is increased. Note that if the contacts would extract electrons perfectly (i.e., $S_n \to \infty$), no such drop would be observed. Instead, a current plateau would be reached (see Appendix, Supporting Information). It should also be remarked that the J_{sc} drop does not depend on the presence of surface states (see Appendix). However, from the simulation shown in Figure 6a and from the experimental data it is clear that for the range of thicknesses used such a feature was not observed.

In addition, our simulations reproduce the overall effect of surface states on the absorber thickness dependence of J_{sc} and V_{oc}, which thereby corroborates assumptions (iii) and (iv). It should be remarked that the effect of surface states becomes even more important when the Co_3O_4 thickness decreases. Indeed, in this case minority carriers are extracted at the Co_3O_4|TiO_2 interface, away from the recombination center. Since the solar cell is illuminated from the TiO_2 side, the effect of traps will be noticeable only if the recombination center is close to the Co_3O_4|TiO_2 interface, i.e., when the thickness of the Co_3O_4 layer is small.

It should also be noted that our model underestimates the J_{sc} and V_{oc} drops induced by the presence of the traps. This may be due to a band shift at the interface between Co_3O_4 and the hole's selective contact. In particular, a high density of trap states may induce Fermi level pinning at the interface Co_3O_4|Au, which would change the position of the band edge and drastically influence the recombination rate at this interface. However, such an effect has not been taken into account here and is out of the scope of this paper.

4. Conclusions

We have demonstrated the improved photovoltaic performance of TiO_2|Co_3O_4|MoO_3 all-oxide heterojunction solar cells fabricated by spray pyrolysis and pulsed laser deposition. By appropriate work function matching between Co_3O_4 and MoO_3, which serve as a recombination contact, we have achieved an open-circuit voltage enhancement of over 200 mV with 50-nm thick MoO_3 as the hole-selective contact (HSC), which is a significant improvement compared to Co_3O_4|Au cells. Using a powerful

combinatorial approach and calculations in this paper, we can adequately describe the behavior of $TiO_2|Co_3O_4|Au$ and $TiO_2|Co_3O_4|MoO_3|Au$ cells. Based on the advanced modeling and calculations proposed here, we have established that MoO_3 not only acts as an efficient HSC but also eliminates the surface recombination at the absorber/metal back contact interface and passivates the surface.

5. Experimental Section

Spray Pyrolysis of TiO_2: Commercially available fluorine-doped SnO_2 (FTO) coated glass substrates (Figure 1a) with a size of 71.2 mm × 71.2 mm, and a sheet resistance of 15 Ω $\square^{-1}$ (TEC 15, Hartford Glass Co. Inc.) were thoroughly washed with soap, rinsed with ethanol and de-ionized water, followed by drying under a dry air stream. Compact TiO_2 layers were deposited by spray pyrolysis, where the substrates were placed onto a Ceran hotplate (Harry Gestigkeit GmbH). A precursor solution of 0.1 M titaniumtetraisopropoxide and 0.1 M acetylacetone in ethanol and isopropanol (mixing ratio 1:1) was sprayed with a pneumatic spray nozzle (Spraying Systems Co.) onto the substrates at a hotplate temperature of 450 °C. The nozzle was mounted onto a commercial *x-y-z* scanner (EAS GmbH);[22,23] and the precursor flow rate of 60 cm^3 h^{-1} was controlled by a syringe pump (Razel Scientific Instruments), while clean dehumidified compressed air at a flow rate of 6 L min^{-1} was used as carrier gas. The *x–y* scan velocity was 30 mm s^{-1}, and the nozzle-to-substrate distance was approximately 6.9 cm. For combinatorial device fabrication a linear thickness gradient (Figure 1b) was produced using a series of spray cycles with a successively decreasing scan area.

Pulsed Laser Deposition of Co_3O_4: Co_3O_4 thin films were deposited onto compact TiO_2 layers with a continuous thickness gradient using a commercial pulsed laser deposition (PLD) system (Neocera) equipped with a KrF excimer laser with an emission wavelength of 248 nm (Coherent Compex Pro 102). The substrate was kept inside the PLD system by a custom-made sample holder with a built-in heater. A total of 30000 incident laser pulses were applied to a commercial Co_3O_4 target (J.Kurt Lesker, purity 99.9%) at a repetition rate of 8 Hz. The energy of the laser was 90 mJ $pulse^{-1}$, corresponding to an energy density of 2 J cm^{-2}. Throughout the deposition the sample was heated to a temperature of 600 °C and maintained at a target-substrate distance of 55 mm and oxygen pressure of 33 mTorr. To attain a continuous thickness gradient, the deposition was carried out without sample rotation (Figure 1c).

MO_3 Pulsed Laser Deposition: A MoO_3 thin film was deposited onto the same Co_3O_4 layer with Au back contacts in a continuous thickness gradient perpendicular to the Co_3O_4 deposition profile using PLD (Figure 1e). In this way we could use the same Co_3O_4 without an additional deposition. A total of 10000 incident laser pulses were applied to a commercial MoO_3 target (J.Kurt Lesker, purity 99.9%) energy of 90 mJ $pulse^{-1}$, at a repetition rate of 8 Hz. The energy of the laser was 90 mJ $pulse^{-1}$, corresponding to an energy density of 2 J cm^{-2}. Throughout the deposition the sample was heated to (400 °C) and maintained at a target-substrate distance of 72 mm and oxygen pressure of 33 mTorr. To attain a continuous thickness gradient the deposition was carried out without sample rotation.

Deposition of Electrical Contacts: For *I–V* characterization the FTO substrate served as a transparent conducting front electrode. A grid of 13 × 13 100-nm thick metal circles with a diameter of 1.8 mm were deposited by sputtering onto the Co_3O_4 layer using a shadow mask and served as back contacts (Figure 1d). To attain good electrical contact to the measurement system, the TiO_2 and Co_3O_4 layers were mechanically removed close to the library edges using a diamond pen, followed by ultrasonic soldering (MBR Electronics) of a thin frame of a soldering alloy around the device library.

After the deposition of a grid of gold contacts on Co_3O_4, the sample was rotated 90° and a thin MoO_3 layer was deposited (as described above) followed by an additional 13 × 13 grid of gold back contacts, offset laterally to form two sets of 169 cells (Figure 1f). [The advantage of this method is that it allows direct comparison between Co_3O_4 cells with and without the MoO_3, since both sets of cells utilize the same Co_3O_4 and TiO_2 layers.]

Structural Characterization: Structural characterization of the photovoltaic (PV) cell libraries were carried out prior to deposition of the back contacts. X-ray diffraction measurements were performed using a Rigaku Smartlab work station with a θ–2θ scan range from 15 to 70° on six different points along the MoO_3 thickness gradient.

Optical Characterization: Optical transmission and reflectance spectra were measured with a home-built mapping system, consisting of a computer controlled *x-y* scanning table) Märzhäuser Wetzlar GmbH & Co. KG) in conjunction with a specular reflectance probe and two integrating spheres, connected by optical fibers to CCD array spectrometers) HR4000, Ocean Optics Inc.). Total transmittance (*TT*), total reflectance (*TR*), and specular reflectance (*SR*) were measured after the deposition of each layer.[27]

Thickness Analysis: The thickness of the TiO_2 layer was determined by using commercially available optical modeling software (CODE), 25 fitting simulated reflection and transmission spectra, in the spectral range 350–1000 nm, to the measured ones with the TiO_2 thickness, d_{TiO_2}, as a fitting parameter. The simulation was based on the OJL interband transition model,[29] and it was validated on different samples by using cross-section scanning electron microscopy (SEM) with a focused ion beam (FIB).

The Co_3O_4 thickness, d_{Co3O4}, was derived from total transmission (*TT*) and total reflectance (*TR*) data at 550 nm, $d_{Co_3O_4} = \alpha\ (563\ nm)^{-1} \log(TT(563\ nm)/(1 - TR(563\ nm)))$ using an absorption coefficient, $\alpha = 1.14 \times 10^4\ cm^{-1}$ at 563 nm (2.2 eV). SEM measurements were carried out on the same points using a Helios 600 system (FEI). The Co_3O_4 thickness derived from the optical measurements was verified with the thickness determination from cross-section SEM measurements taken at the maximum thickness of the deposition profile. The measured and calculated thicknesses were in good agreement with each other with a difference of less than 5 nm.

Solar Cell Characterization: The *I–V* characteristics of all 169 solar cells were measured with a home-built automated scanning *I–V* system consisting of a Keithley 2400 source meter, an *x–y* scanning table (Märzhäuser Wetzlar GmbH & Co. KG) in conjunction with a motorized z-arm Olympus/Märzhäuser Wetzlar GmbH & Co. KG) and a laser pumped Xe lamp (LDLS, from Energetics Co.), which was coupled through an optical fiber to the scanning stage. The solar-cell device library was placed onto the *x–y* stage and mechanically clamped using metal clips, which also provided the electrical connection between the FTO via the soldered metal frame, and the source meter for electrical measurements Keithley 2400). Temporary electrical contact to each individual solar cell was established by a gold-plated spring-loaded tip (Ingun Prüfmittelbau GmbH), mounted onto the motorized z-arm, touching the back-contact metal patch for the duration of the measurement. After each measurement was completed, the tip was lifted and the *x–y* scanning table moved the library to the next contact. For each point the *I–V* curve was measured twice, in ascending and descending scan direction, to exclude capacitive effects due to charge trapping. Solar cells that showed a difference of more than 15% in the open circuit voltage (V_{oc}), short circuit current (J_{sc}), or the fill factor were not considered for further analysis, as well as *I–V* curves that showed less than three measurement points in the quadrant of photovoltaic action.[28,30]

Data Acquisition: LabVIEW programming was used to control the scanning system for optical and solar cell characterizations. Solar cell parameters were extracted by data extraction software. Matlab graphical software was used for the graphical data presentation.

Acknowledgments

This project received funding from the Israeli National Nanotechnology Initiative (INNI, FTA project), and from the European Commission under the FP7 AllOxidePV project entitled *"Novel Composite Oxides*

by Combinatorial Material Synthesis for Next Generation All-Oxide-Photovoltaics", Number 309018. Funding from the European Union Seventh Framework Program [FP7/2007–2013] under grant agreement 316494 is also acknowledged. This project also received funding from the European Union's Horizon 2020 research and innovation programme under the Marie Sklodowska-Curie grant agreement No 659774.

Received: July 26, 2015
Revised: September 10, 2015
Published online:

[1] R. Nechache, C. Harnagea, S. Li, L. Cardenas, W. Huang, J. Chakrabartty, F. Rosei, *Nat. Photon.* **2015**, *9*, 61.
[2] P. Patil, L. Kadam, C. Lokhande, *Thin Solid Films* **1996**, *272*, 29.
[3] a) M. Long, W. Cai, J. Cai, B. Zhou, X. Chai, Y. Wu, *J. Phys. Chem. B* **2006**, *110*, 20211; b) Q. Xiao, J. Zhang, C. Xiao, X. Tan, *Catal. Commun.* **2008**, *9*, 1247; c) X. Lou, J. Han, W. Chu, X. Wang, Q. Cheng, *Mater. Sci. Eng. B* **2007**, *137*, 268; d) L. Xi, P. D. Tran, S. Y. Chiam, P. S. Bassi, W. F. Mak, H. K. Mulmudi, S. K. Batabyal, J. Barber, J. S. C. Loo, L. H. Wong, *J. Phys. Chem. C* **2012**, *116*, 13884; e) P. F. Newhouse, B. A. Parkinson, *J. Mater. Chem. A* **2015**, *3*, 5901.
[4] B. Kupfer, K. Majhi, D. A. Keller, Y. Bouhadana, S. Rühle, H. N. Barad, A. Y. Anderson, A. Zaban, *Adv. Energy Mater.* **2015**, *5*, 1401007.
[5] a) H.-K. Kim, T.-Y. Seong, J.-H. Lim, W. Ii Cho, Y. Soo Yoon, *J. Power Sources* **2001**, *102*, 167; b) S. Kandalkar, J. Gunjakar, C. Lokhande, *Appl. Surf. Sci.* **2008**, *254*, 5540.
[6] H.-J. Nam, T. Sasaki, N. Koshizaki, *J. Phys. Chem. B* **2006**, *110*, 23081.
[7] a) C. Chen, A. Buysman, E. Kelder, J. Schoonman, *Solid State Ion.* **1995**, *80*, 1; b) K.-S. Han, S. W. Song, M. Yoshimura, *J. Am. Ceram. Soc.* **1998**, *81*, 2465.
[8] M. T. Greiner, Z.-H. Lu, *NPG Asia Mater.* **2013**, *5*, e55.
[9] P. Schulz, S. R. Cowan, Z. L. Guan, A. Garcia, D. C. Olson, A. Kahn, *Adv. Funct. Mater.* **2014**, *24*, 701.
[10] M. T. Greiner, L. Chai, M. G. Helander, W. M. Tang, Z. H. Lu, *Adv. Funct. Mater.* **2013**, *23*, 215.
[11] D. Y. Kim, J. Subbiah, G. Sarasqueta, F. So, H. Ding, Irfan, Y. Gao, *Appl. Phys. Lett.* **2009**, *95*, 093304.
[12] C. Girotto, E. Voroshazi, D. Cheyns, P. Heremans, B. P. Rand, *ACS Appl. Mater. Interfaces* **2011**, *3*, 3244.
[13] F. Zhang, D. Zhao, Z. Zhuo, H. Wang, Z. Xu, Y. Wang, *Sol. Energy Mater. Sol. Cells* **2010**, *94*, 2416.
[14] K. H. Wong, K. Ananthanarayanan, J. Luther, P. Balaya, *J. Phys. Chem. C* **2012**, *116*, 16346.
[15] D. W. Zhao, P. Liu, X. W. Sun, S. T. Tan, L. Ke, A. K. K. Kyaw, *Appl. Phys. Lett.* **2009**, *95*, 153304.
[16] a) J. Bullock, A. Cuevas, T. Allen, C. Battaglia, *Appl. Phys. Lett.* **2014**, *105*, 232109; b) C. Battaglia, X. Yin, M. Zheng, I. D. Sharp, T. Chen, S. McDonnell, A. Azcatl, C. Carraro, B. Ma, R. Maboudian, R. M. Wallace, A. Javey, *Nano Lett.* **2014**, *14*, 967.
[17] C. Battaglia, S. M. De Nicolas, S. De Wolf, X. Yin, M. Zheng, C. Ballif, A. Javey, *Appl. Phys. Lett.* **2014**, *104*, 113902.
[18] J. Subbiah, P. M. Beaujuge, K. R. Choudhury, S. Ellinger, J. R. Reynolds, F. So, *Org. Electron.* **2010**, *11*, 955.
[19] D. W. Zhao, S. T. Tan, L. Ke, P. Liu, A. K. K. Kyaw, X. W. Sun, G. Q. Lo, D. L. Kwong, *Sol. Energy Mater. Sol. Cells* **2010**, *94*, 985.
[20] D. W. Zhao, X. W. Sun, C. Y. Jiang, A. K. K. Kyaw, G. Q. Lo, D. L. Kwong, *Appl. Phys. Lett.* **2008**, *93*, 083305.
[21] M. Kroger, S. Hamwi, J. Meyer, T. Riedl, W. Kowalsky, A. Kahn, *Appl. Phys. Lett.* **2009**, *95*, 123301.
[22] J. Meyer, S. Hamwi, M. Kröger, W. Kowalsky, T. Riedl, A. Kahn, *Adv. Mater.* **2012**, *24*, 5408.
[23] S. McDonnell, A. Azcatl, R. Addou, C. Gong, C. Battaglia, S. Chuang, K. Cho, A. Javey, R. M. Wallace, *ACS Nano* **2014**, *8*, 6265.
[24] Y.-J. Cheng, C.-H. Hsieh, Y. He, C.-S. Hsu, Y. Li, *J. Am. Chem. Soc.* **2010**, *132*, 17381.
[25] H. Park, P. R. Brown, V. Bulović, J. Kong, *Nano Lett.* **2011**, *12*, 133.
[26] a) M. Woodhouse, B. Parkinson, *Chem. Soc. Rev.* **2009**, *38*, 197; b) D. A. Keller, A. Ginsburg, H.-N. Barad, K. Shimanovich, Y. Bouhadana, E. Rosh-Hodesh, I. Takeuchi, H. Aviv, Y. R. Tischler, A. Y. Anderson, *ACS Combinatorial Sci.* **2015**, *17*, 209; c) M. Woodhouse, G. Herman, B. Parkinson, *Chem. Mater.* **2005**, *17*, 4318.
[27] A. Y. Anderson, Y. Bouhadana, H.-N. Barad, B. Kupfer, E. Rosh-Hodesh, H. Aviv, Y. R. Tischler, S. Rühle, A. Zaban, *ACS Combinatorial Sci.* **2014**, *16*, 53.
[28] S. Rühle, A. Y. Anderson, H.-N. Barad, B. Kupfer, Y. Bouhadana, E. Rosh-Hodesh, A. Zaban, *J. Phys. Chem. Lett.* **2012**, *3*, 3755.
[29] S. K. O'Leary, S. Johnson, P. Lim, *J. Appl. Phys.* **1997**, *82*, 3334.
[30] H.-N. Barad, S. Rühle, Y. Bouhadana, A. Y. Anderson, A. Zaban, *Phys. Chem. Chem. Phys.* **2014**, *16*, 7066.
[31] L. Bertoluzzi, P. P. Boix, I. Mora-Sero, J. Bisquert, *J. Phys. Chem. C* **2014**, *118*, 16574.

